Hindawi
Geofluids
Volume 2022, Article ID 2033679, 12 pages
https://doi.org/10.1155/2022/2033679

Research Article

Experimental Study on Dynamic Response and Damage Evolution of Coal under Shocks by Multiple High-Pressure Air Blasting

Shaoyang Yan,[1] **Xiaolin Yang**,[1,2] **Huaibao Chu**,[1,2] **Jinxing Wang**,[1,2] **Chang Wang**,[1] **and Mengfei Yu**[1]

[1]*School of Civil Engineering, Henan Polytechnic University, Jiaozuo 454000, China*
[2]*Underground Engineering and Disaster Prevention Key Laboratory of Henan Province, Henan Polytechnic University, Jiaozuo 454000, China*

Correspondence should be addressed to Xiaolin Yang; yangxl@hpu.edu.cn

Received 23 January 2022; Revised 20 February 2022; Accepted 18 April 2022; Published 16 May 2022

Academic Editor: Liang Xin

To explore the dynamic response and damage evolution of coal under multiple high-pressure air blasting (HPAB), simulated coal specimens were used in the HPAB experiments, and the variation laws of stress field, vibration field, damage field, and cumulative fracture failure process in specimens were analyzed from a macro point of view. A scanning electron microscope (SEM) and mercury intrusion porosimetry (MIP) were used to observe the pore distribution near the blasthole of the specimen and analyze the variation law of pore structure parameters under multiple HPAB from the microscopic point of view. The test results show that (1) the stress wave generated by HPAB has a great impact on the near zone. After multiple HPAB, the damage value at the place 50 mm away from the blasthole increases by 3.91 times compared with the one shock from HPAB, and the strain peak and vibration velocity are reduced by 17.86% and 63.05%, respectively. With the increase of distance, the internal damages of the specimens in the middle and far zones are mainly driven by the stress wave and the high-pressure air, and the strain peak, vibration velocity, and damage degree gradually decrease. (2) With the increase of shock times in HPAB tests, the stress wave attenuation index decreases at first and then increases, and the damages degree of the middle and far zones increase slowly in the first few shocks and then increase rapidly. The site coefficient (k) shows an overall decreasing trend, whereas the attenuation coefficient (α) tends to increase. (3) The multiple HPABs have a great impact on the pore structure of the specimens. Compared with unshocked specimen, the cumulative mercury injection and pore volume increased by 152.04% and 135.05%, respectively. The number of connecting pores with large pore diameter is significantly increased. The multiple HPAB can effectively improve the pore and fracture structure in the specimens and form a relatively developed fracture network channel. The study results have certain guiding value for solving practical engineering problems of low extraction efficiency in low permeability coal seams.

1. Introduction

Coalbed methane is a kind of clean energy with rich reserves and wide distribution, which is stored in coal seams and coal measures strata [1–3]. However, the leakage of coalbed methane will cause serious hazards such as explosion and gas outbursts, resulting in unexpected personal casualties and economic losses, which will seriously impact the healthy and stable development of the coal industry to a certain extent [4–6]. Therefore, the efficient extraction of coalbed methane can not only reduce mining accidents and ensure mine safety production, but also increase the supply of clean energy and promote the sustainable development of a low-carbon economy and green environment [7, 8]. Generally, the techniques for improving the permeability of low permeability coal seams can be divided into anhydrous fracturing and hydraulic fracturing. The hydraulic fracturing technology is relatively mature for the permeability enhancement of low-permeability coal

seams. However, it has some certain limitations, such as the large consumption of water resources and the water lock reaction and water sensitivity damage to the reservoir caused by the invasion and retention of water [9–11].

In recent years, with the increasingly prominent environmental problems, the society has been increasingly focused on green development [12]. It is worth mentioning that high-pressure gas fracture is a new anhydrous fracturing technology, which mainly includes liquid CO_2 phase change fracture, high-energy gas fracture, and high-pressure air fracture. It is booming in the application in unconventional gas extraction [13–16], tunnel engineering [17, 18], foundation pit excavation [19, 20], quarry [21, 22], and other fields, based on the characteristics of environmental protection, energy-saving, simple operation, high efficiency, and safety [23, 24]. In addition, there are a series of reports on the theory of high-pressure gas fracturing technology. Some scholars researched the cracking mechanism and crack propagation of high-pressure gas by the means of laboratory tests [25–28] and numerical simulation [29, 30]. To further explore the peak pressure in the blasthole and its cracking mechanism and dynamic response, some scholars studied the pressure distribution in the hole through theoretical analysis [31, 32], sensor test [33, 34], and numerical simulation [35, 36]. Based on the difficulties to measure the change of stress field in coal and rock mass, some scholars studied the change of stress field using numerical simulation and the mathematical model. For example, Zhu et al. [37] and Wei et al. [38] used the numerical simulation method to analyze the distribution of stress waves around the borehole and found that the peak stress decreased with the increase of propagation distance. Liu et al. [39] and Song et al. [40] used the stress wave dispersion equation and mathematical model to reveal the changes of the stress field in coal caused by high-pressure gas jet erosion on coal surface. In addition, some studies showed that [41, 42], compared to explosive blasting, high-pressure gas fracturing had a shorter vibration wave duration, faster vibration velocity attenuation, fewer high-frequency components, and a more significant damping effect in the medium and far range under the same energy. However, the research on the high-pressure gas fracturing technology is not perfect, and there are few studies concerning the dynamic response of coal in the process of high-pressure gas cracking, especially the response of cumulative damage characteristics and vibration propagations.

Therefore, in this paper, we are dedicated to exploring the change of stress field, cumulative damage evolution, and dynamic response of coal under multiple HPAB with a self-designed HPAB test system. Besides, the pore size distribution and pore structure evolution of specimens before and after HPAB are analyzed. The influence effect of shock times on the micropore structure of specimens is explored. Overall, the results provide a theoretical and experimental basis for improving coal seam permeability.

2. Experimental Materials and Methods

2.1. Experimental Materials and Production of Specimen. Because of the particularity and complexity of physical and mechanical properties of coal, there are many inconvenient factors indirectly using coal in the HPAB test to study its stress characteristics and dynamic response (such as specimen processing and sensors embedding). Therefore, according to the similarity theory, artificially simulated coal close to hard coal is selected for the HPAB test [43].

The specimen is mainly composed of aggregate, cementitious material, and other materials. The specific details of the components, parameters, and functions are listed in Table 1. The mix ratio and mechanical properties of simulated coal are shown in Table 2.

According to the methods above, three parallel specimens with a size of $500 \times 300 \times 300$ mm were made. During the parallel specimen preparation, a blasthole with a depth of 200 mm and a diameter of 12 mm need to be reserved from one end of the specimen. Additionally, strain bricks with a size of $20 \times 20 \times 20$ mm need to be embedded, respectively, at the intersection of 50 mm, 110 mm, 210 mm, and 320 mm from the blasthole and 120 mm from the bottom of the specimen.

2.2. Experiment Methods

2.2.1. HPAB Experiment. The specimens were maintained for 28 days under standard curing conditions, the HPAB test was carried out under the pressure of 10 MPa with the self-designed HPAB system, two-direction loading, and the in-site stress $\sigma_1 = \sigma_2 = 4$ MPa are applied to the specimens. The HPAB system consists of four parts, including the gas pressurization system, the high-pressure gas release control system, the specimen two-direction loading system, and the data acquisition system. As shown in Figure 1, the surface around the specimen was coated with a layer of the coupling agent with a thickness of 4-6 mm to avoid the error caused by boundary effects.

The PVDF signal sensor was fixed to the bottom of the blasthole by glue, and the fracturing pipe was fixed at a height 50 mm away from the bottom of the blasthole by planting reinforcement glue. The terminal of the test system (the YE5853A charge amplifier and DH5922N dynamic strain gauge) was used to estimate the variations of the pressure in the blasthole and the changes of the stress field in the specimen. A NM-4A type nonmetal ultrasonic testing instrument was used to measure the acoustic velocity of the specimen before and after each shock of HPAB. A TC-4850 blasting vibration meter is used to detect the vibration velocity and frequency. Furthermore, this experiment involves 7 test points of the NM-4A type nonmetal ultrasonic detector and 4 test points of the TC-4850 blasting vibrometer in total, which were located 0 mm, 50 mm, 100 mm, 150 mm, 200 mm, 250 mm, and 300 mm away from the blasthole and 50 mm, 110 mm, 170 mm, and 310 mm away from the blasthole, respectively. The layout of measuring points is shown in Figure 2.

2.2.2. Mercury Intrusion Porosimetry (MIP) Experiment. The failure specimens with a mass of about 5 g were taken from the same section near the blasthole unshocked specimen and after the one shock, three shocks, and five shocks from HPAB for the MIP test as shown in Figure 3(a). The pore structure and pore size distribution in the specimen were

Table 1: Physical properties and functions of test materials.

Classification	Samples	Physical parameter	Function
Aggregate	Sand	With the particle size is less than 6 mm	Control the mechanical properties of simulated coal
Cementitious material	P.O.32.5 Portland cement	With the density of 3.0~3.15 g/cm^3	
	Gypsum	With the Mohs hardness of 3~3.5, the density of 2.8~3.0 g/cm^3, and the fineness of 400 mesh	
Other materials	Mica	With the particle size of 10~15 mesh, which is a flake thin layer structure	Control the random distribution of cracks in simulated coal
	Perlite	A natural silicate mineral with the particle size of 2~3 mm and a unit weight of 80~200 kg/m^3	Control the formation of weak surface structure in simulated coal
	Foaming agent ($NaHCO_3$)	The white crystalline powder with the density of 2.16 g/cm^3, which is easy to decompose and produce gas in a humid environment	Simulate the gas

Table 2: Mix ratio and mechanical properties of simulated coal.

A mix ratio of specimen Cement:sand:gypsum:water:perlite:foaming agent:mica	Uniaxial compressive strength (MPa)	Density (g/cm^3)	Elastic modulus (GPa)	Wave velocity (m/s)
1 : 2.8 : 0.14 : 0.43 : 0.02 : 0.035 : 0.02	12.18	1.526	2.52	2152

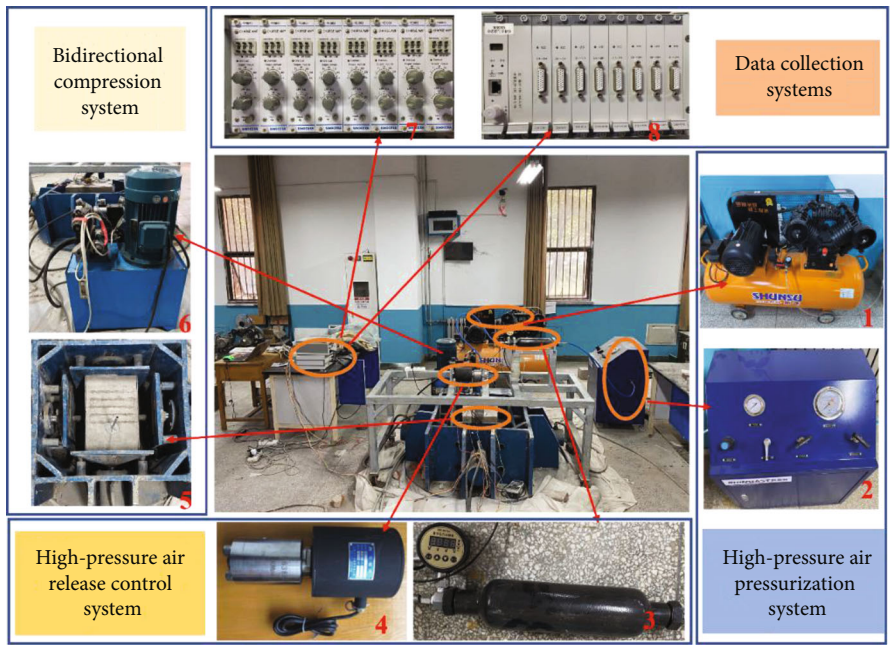

Figure 1: HPAB test system. 1: air compressor; 2: air booster pump; 3: autoclave; 4: dynamic strain gauge; 4: high-speed solenoid valve; 5: bidirectional compression system; 6: confining pressure device; 7: Ye5853A signal amplifier; 8: DH5922N dynamic strain gauge.

analyzed by the AutoPore IV 9500 automatic mercury intrusion instrument as shown in Figure 3(b). The test procedure is as follows: firstly, specimens are dried to constant weight at 60°C. Secondly, put 2~3 g sample into the dilatometer for vacuum sealing. Thirdly, put the dilatometer at the low-pressure port and high-pressure port of the mercury porosimeter for pressurization. Finally, the pore structure and pore size distribution are analyzed by mercury injection pressure, respectively.

2.2.3. Scanning Electron Microscope (SEM) Experiment. The failure specimens with a size of about 1cm^3 were taken from the same section near the blasthole before and after the HPAB test for the SEM test. The position of the specimen

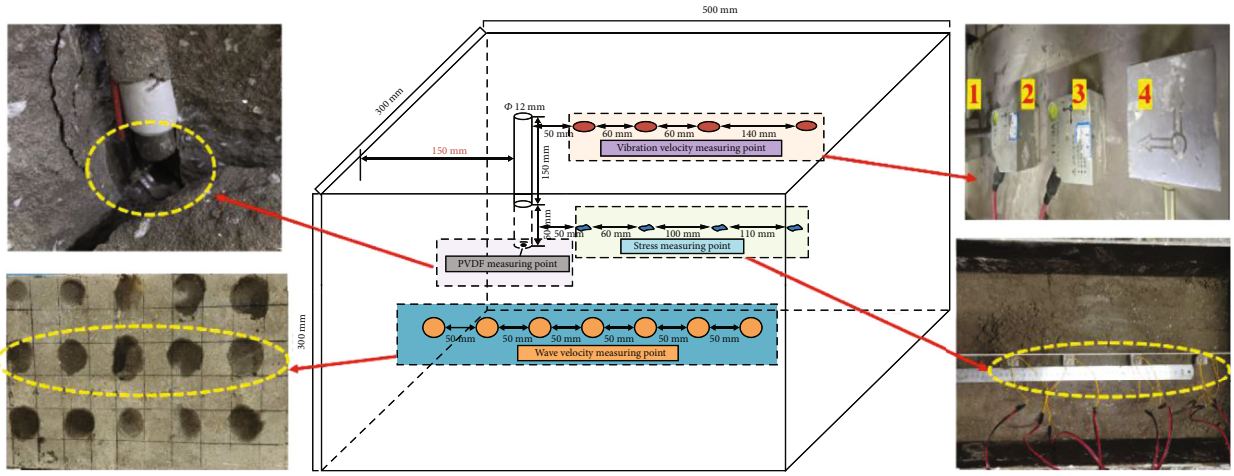

Figure 2: The layout of measuring points.

is shown in Figure 3(a). During the test, the specimen is fixed on the sample table with conductive adhesive. The sample table for fixing the sample was placed in the ion sputtering equipment for gold plating. Place the gold-plated sample on the sample pedestal, close the cabin door, and conduct a vacuum pumping operation. When the vacuum pressure reaches the specified pressure, select the appropriate magnification and brightness contrast for the SEM test, as shown in Figure 3(c).

3. Experiment Results and Analysis of Multiple HPAB Tests

The three specimens were broken after the five shock times, the six shock times, and the six shock times in HPAB tests, respectively. The results were analyzed by taking the five shock times failure as an example. The five aspects including the pressure time history curve, variation of the stress field in the specimen, cumulative damage evolution, characteristic of vibration velocity, and failure process of the specimen were further discussed and analyzed.

3.1. Pressure Time History Curve. The pressure time history curve in the blasthole within 10 ms after HPAB was tested by the PVDF pressure sensor. As shown in Figure 4, the curve can be divided into three main stages: sharp rise stage, sharp decline stage, and slow decline stage. In order to better understand the peak pressure change in the blasthole, the data within 1 ms of HPAB tests were intercepted and analyzed.

3.1.1. Sharp Rise Stage (AB Segment). In a depressurization-expansion process, by controlling the high-speed solenoid valve to release high-pressure air instantaneously, the blasthole reaches high pressure, and the internal pressure of the blasthole increases instantaneously. The stagnation point pressure of the blasthole wall is calculated by the formula as below:

$$p = p_0 + c^2\rho_0 \frac{\{0.7/((kH/r_0)+0.3)\}\Delta\rho_0}{\{0.7/((kH/r_0)+0.3)\}\Delta\rho_0 + \rho_0}. \quad (1)$$

In the formula, P is the stagnant point pressure at the bottom of the blasthole, P_0 is the external pressure of high-pressure trachea, c is the acoustic velocity, ρ_0 is the gas density outside high-pressure trachea, $\Delta\rho_0$ is the gas density difference, H is the distance between the impact position of the high-pressure air and the wall of the blasthole, r_0 is the radius of the high-pressure trachea, and k is the coefficient.

3.1.2. Sharp Decline Stage (BC Segment). The pressure P generated by HPAB may not reach the compressive strength, but the shear stress and tensile stress of the pressure P are greater than the dynamic tensile strength of the specimen. Suffering the stronger stress, the medium in the specimen appears dislocated and sliding, resulting in the immediate leakage of the pressure in the blasthole from the pores and cracks between the medium in the specimen.

3.1.3. Slow Decline Stage (CD Segment). At this stage, with the dispersion of high-pressure air in the crack, the pressure in the borehole gradually decreased until it is balanced with the gas pressure in the fracture of the sample.

3.2. Analysis of Stress Field Variation. The results of the radial strain peak at each measuring point of the specimen are shown in Table 3. The fitting curve between the strain peak and the distance under multiple HPAB tests are shown in Figure 5.

The conclusions drawn from Table 3 and Figure 5 are as follows:

The strain peak decreased with the increase of shock times in HPAB tests. The internal stress wave attenuation curve of the specimen under multiple HPAB tests is roughly similar. The strain decays as a power function with the increase of the distance between the measuring points. The attenuation indices of stress waves are 1.304, 1.161, 1.431, 1.511, and 1.728, respectively.

The attenuation index of the stress wave decreases first and then increases; that is, the propagation velocity of the stress wave in the specimen decreases first and then increases under multiple HPAB tests. The main reason for this phenomenon is that the energy generated by the first two shock from HPAB densifies the original micropores of

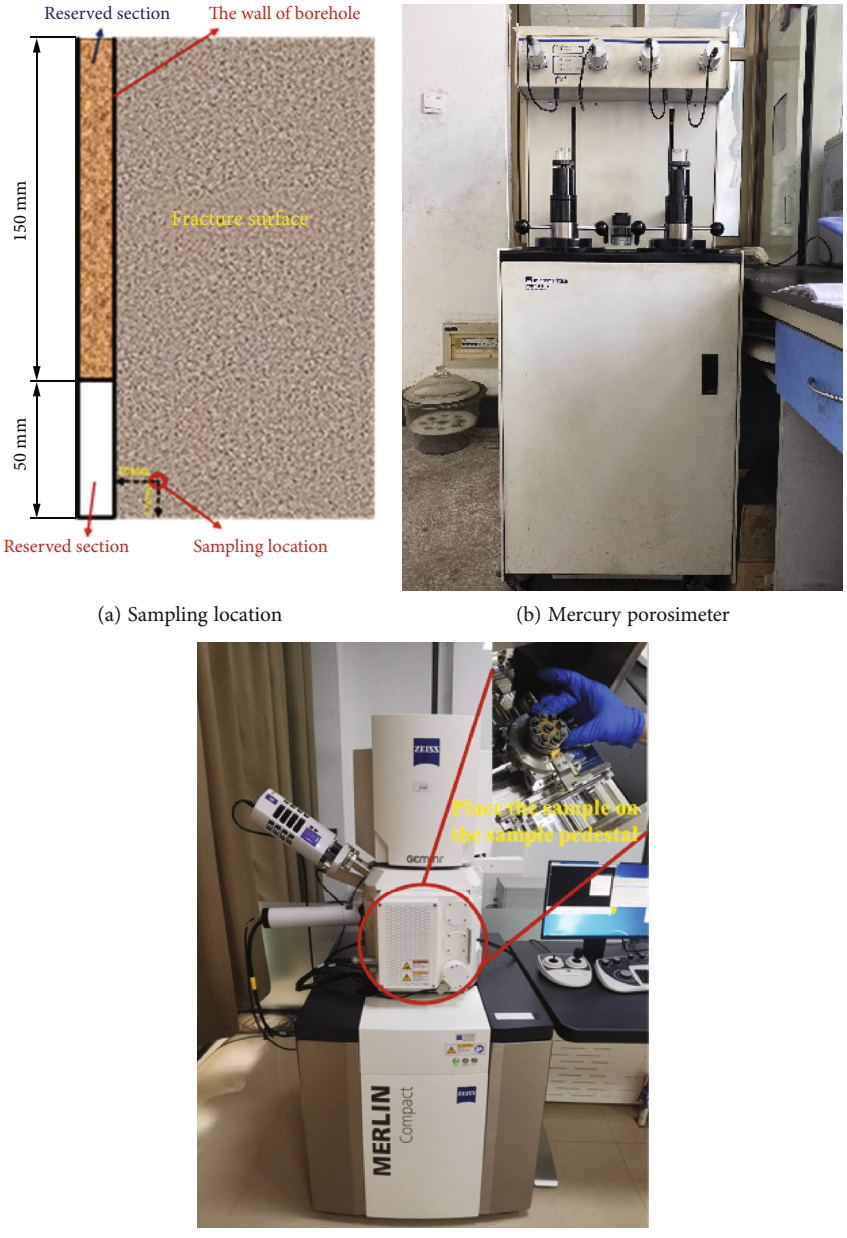

(a) Sampling location

(b) Mercury porosimeter

(c) Scanning electron microscope

Figure 3: Sampling location and test instrument.

the specimen and reduces the energy consumption of stress wave propagation. With the increase of shock times in HPAB tests, under the action of stress wave, the internal pores and cracks of the specimen are further developed, resulting in the deterioration of the integrity of the specimen. The stress wave encounters different wave impedance interfaces during the propagation process, resulting in the increase of energy consumption and attenuation speed of the stress wave.

3.3. Analysis of Damage Evolution. The damage of the media can be obtained by the calculation of ultrasonic, which is characterized by D. Meanwhile, the damage (D_i) caused by multiple HPAB tests can be calculated by the following formula:

$$D_i = 1 - \left(\frac{V_i}{V_0}\right)^2. \tag{2}$$

In the formula, D_i is the damage amount of the specimen under the ith HPAB, V_i is the ultrasonic velocity of the specimen after the ith HPAB, and V_0 is the acoustic velocity of the specimen before HPAB.

The damage results of each measuring point are calculated according to the measured acoustic velocity, as shown in Table 4. The cumulative damage curves of the specimen after multiple HPAB test are shown in Figure 6(a), and the relationship curve between damage value and HPAB times is shown in Figure 6(b).

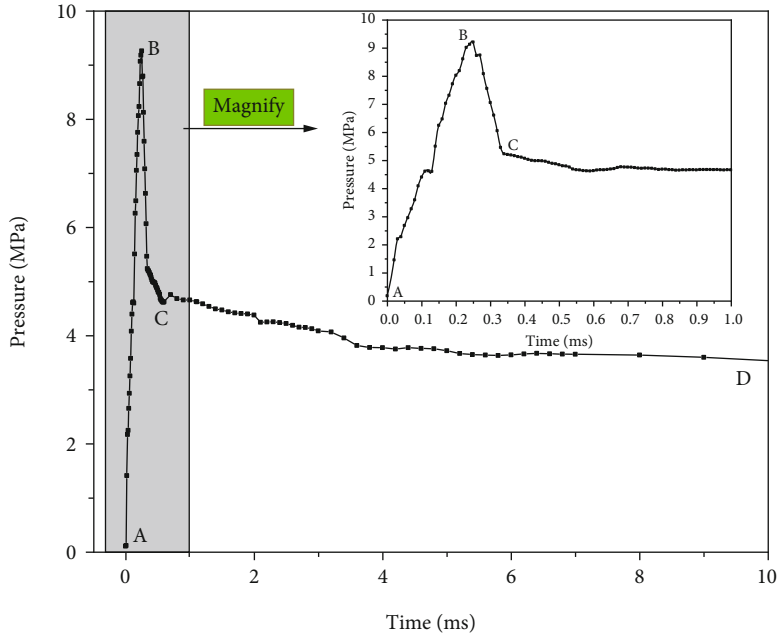

Figure 4: Pressure time history curve of HPAB.

Table 3: The results of radial strain peak at each measuring point.

Times	Radial strain peak at each measuring point/uε			
	50 mm	110 mm	210 mm	320 mm
1	2573.78	959.84	384.69	184.54
2	2565.38	1055.97	460.68	289.91
3	2744.86	857.13	368.06	225.69
4	2856.14	843.59	278.57	227.66
5	3031.82	763.31	278.81	147.78

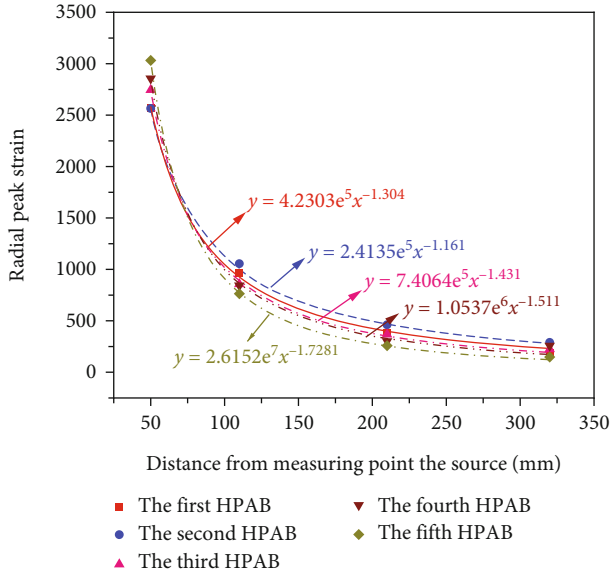

Figure 5: The fitting curve between the strain peak and the distance.

Table 4: The damage results of different points of the specimen under multiple HPAB.

Times	Distance of measuring point/mm						
	0	50	100	150	200	250	300
1	0.108	0.056	0.037	0.018	0.011	0.008	0
2	0.161	0.092·	0.074	0.033	0.012	0.008	0.006
3	0.193	0.156	0.086	0.041	0.020	0.011	0.006
4	0.282	0.213	0.147	0.096	0.051	0.017	0.012
5	0.351	0.275	0.208	0.153	0.136	0.074	0.023

As can be seen from Figure 6, the damage near the blasthole decreases rapidly, whereas the damage decreases gradually with the increase of distance. In addition, with the increase of the shock times in HPAB tests, the damage near the blasthole will increase at an exponential rate. However, in the middle and far zones, the damages of the first two HPAB tests increased slowly, and the damages of the following three HPAB tests increased rapidly.

The failure modes of HPAB on the specimen are mainly divided into the dynamic loading stages under the action of stress wave and the quasi-static loading stages of high-pressure air penetration. Before the macrofracture, the damage near the blasthole is mainly caused by the stress wave. With the increase of distance from the blasthole, the stress wave decays rapidly. The damages in the middle and far zones are mainly caused by stress waves and high-pressure air infiltration disturbance. The energy carried by the stress wave is so large that it makes a large damage zone near the blasthole. The stress wave in the middle and far zones and the penetration of high-pressure air lead to the stress concentration at the tip of the initial pore, resulting in

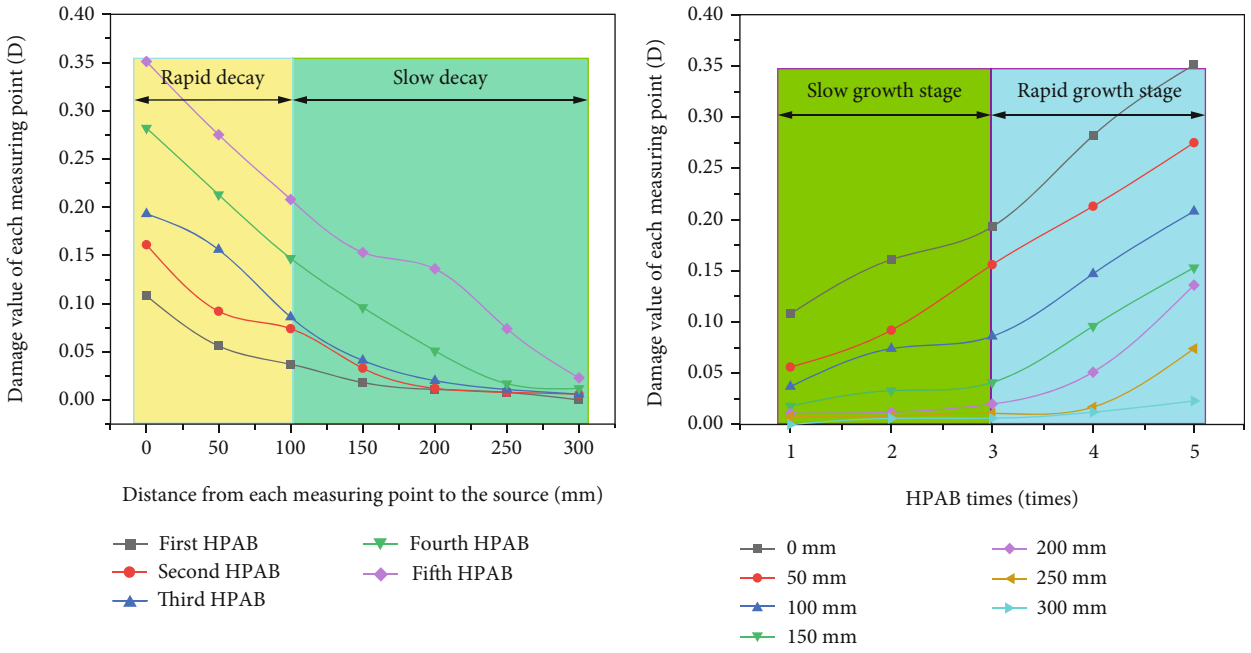

(a) The cumulative damage curve of the specimen after multiple HPAB

(b) The change curve between damage value and HPAB times

Figure 6: Cumulative damage curve of the specimen under multiple HPAB tests.

dislocation and slip between media particles, and the generation of various microdamages, which is the main reason for the slow growth rate of damage factors in the early stage. With the increase of shock times in HPAB tests, the cumulative effect of various microdamage becomes gradually significant, which leads to the rapid growth of damage in the later stage.

3.4. Characteristic Analysis of Vibration Velocity. The total energy of HPAB is equivalent to explosive explosion energy by the TNT equivalent method, and the vibration characteristics caused by the HPAB test are analyzed using the Sadovsky formula. The expression is shown in the formula:

$$V = K\left(\frac{\sqrt[3]{W_{TNT}}}{R}\right)^{a}, \tag{3}$$

$$W_{TNT} = \frac{U_g}{Q_{TNT}}, \tag{4}$$

$$U_g = \frac{PV_1}{\gamma - 1}\left[1 - \left(\frac{0.1013}{P}\right)^{(\gamma-1)/\gamma}\right] \times 10^3. \tag{5}$$

In the formula, V is the peak vibration velocity, W_{TNT} is the TNT equivalent of high-pressure air, K is the site coefficient, α is the attenuation coefficient, U_g is the high-pressure air, Q_{TNT} is the energy of 1 g TNT, 4250 J/g, P is the absolute pressure of the gas, V_1 is the amount of high-pressure gas, and γ is the adiabatic coefficient of the gas.

After continuous monitoring and recording of multiple HPAB tests, the vibration velocity in the Z direction of each measuring point is obtained, as shown in Table 5. The relationship curve between peak vibration velocity and distance

Table 5: Vibration velocity results of each measuring point under multiple HPAB tests(cm/s).

Times	Distance of each measuring point/mm			
	50 mm	110 mm	170 mm	310 mm
1	12.0910	8.9388	5.6011	3.4726
2	10.8377	6.5113	3.5221	2.0318
3	6.8987	4.4675	2.784	1.8943
4	7.1227	5.0010	2.8509	0.8065
5	4.4675	1.5223	1.0960	0.6423

is shown in Figure 7(a). The relationship curve between vibration velocity and HPAB times is shown in Figure 7(b).

It can be concluded from Figure 7(a) that the vibration velocity decreases with the increase of distance. Among them, the vibration velocity near the blasthole attenuates rapidly. With the increase of distance from the blasthole, the vibration velocity attenuates slowly. The site coefficient (k) shows an overall attenuation trend, whereas the attenuation coefficient (α) trend is increasing. The main reason is that with the increase of the shock times in HPAB tests, the development and deterioration degree of pores in the specimen continues to increase. The energy is carried by the shock seismic wave that passes through the pores in the specimen, which causes the reflection and diffraction of the wave. In this process, a large amount of energy is consumed, and the vibration velocity near the hole decays quickly. With the increase of distance from the blasthole, the vibration velocity decays slowly.

It can be concluded from Figure 7(b) that the vibration velocity has an attenuation trend in varying degrees with the increase of shock times in HPAB tests. At 50 mm and

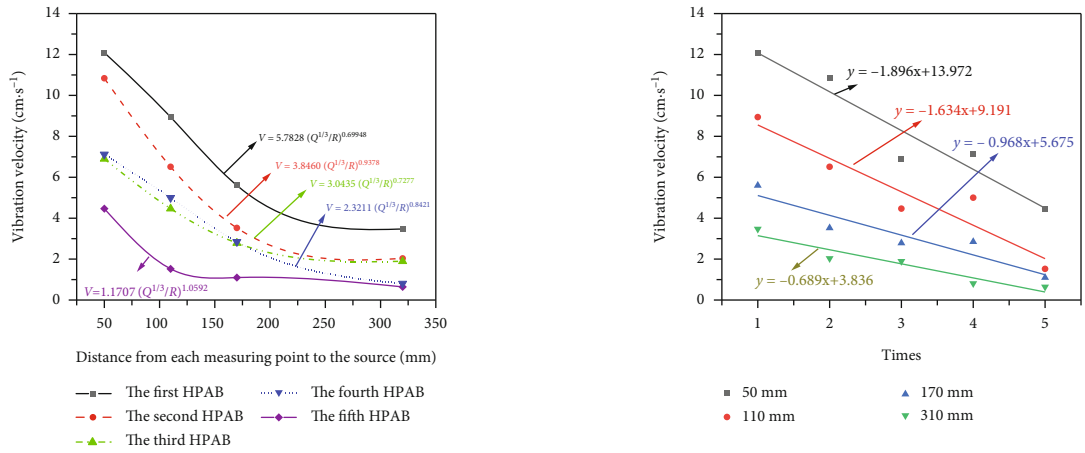

(a) The relationship curve between peak vibration velocity and distance (b) The relationship curve between vibration velocity and HPAB times

Figure 7: The curve of vibration velocity under multiple HPAB tests.

110 mm near the blasthole, the attenuation amplitude of vibration velocities are large; the fitting slopes are -1.896 and -1.634, respectively. The peak value of vibration velocities decreases from 12.0910 cm/s to 4.4675 cm/s and 8.9388 cm/s to 1.5223 cm/s, respectively. The attenuation amplitude of vibration velocities are small in the middle and far zones of 170 mm and 310 mm; the fitting slopes are -0.968 and -0.689, respectively. The peak value of vibration velocity attenuates from 5.6011 cm/s to 1.0960 cm/s and 3.4726 cm/s to 0.6423 cm/s, respectively.

3.5. Analysis of Cumulative Fracture Failure Process. The cumulative fracture process of the specimen under multiple HPAB tests is shown in Figure 8.

It can be seen from Figure 8 that when the first HPAB test is carried out, cracks begin to appear around the blasthole. With the increase of shock times in HPAB tests, the macrodevelopment range of cracks becomes larger. What is more, the specimen is broken after the 5th HPAB test, with 4 irregular main cracks on the surface of the specimen.

There are a lot of uneven microcracks, micropores, and other defects in the specimen, which will be intensified by stress waves to form microdamage distributed with time and space. With the increase of shock times in HPAB tests, when the cumulative damage dynamic intensity factor at the tip of microcracks reaches its dynamic fracture toughness, the randomly distributed microcracks nucleate, expand, and connect to form a macrocrack region until fracture failure.

4. Microcumulative Damage Mechanism Analysis of Multiple HPAB Tests

The mercury intrusion and retraction curve and pore size distribution of specimens under multiple HPAB tests are shown in Figure 9. The comparison of SEM images under multiple HPAB tests is shown in Figure 10.

The peaks of cumulative mercury intrusion of the unshocked specimen after the one shock, three shocks, and five shock from HPAB are 0.098 ml/g, 0.121 ml/g, 0.188 ml/g, and 0.247 ml/g, respectively. The peaks of the pore volume are 0.097 ml/g, 0.138 ml/g, 0.165 ml/g, and 0.228 ml/g, respectively. Compared with unshocked specimen, cumulative mercury intrusion after the one shock, three shocks, and five shocks from HPAB increased by 23.47%, 91.84%, and 152.04%, respectively. The pore volume increased by 42.27%, 70.10%, and 135.05%, respectively.

There is an overlap between the mercury intrusion and mercury retraction curves of the specimen before the HPAB test, which indicates that there are fewer semiclosed pores and open pores and more closed pores in the specimen. There is a hysteresis loop between mercury intrusion and mercury retraction curves of the specimen after the HPAB test. The size of the hysteresis loop increases with the increase of shock times in HPAB tests. Through the above results, it is found that the shock times have a great impact on pore development. With the increase of shock times in HPAB tests, the closed pores evolve to semiclosed pores and open pores Figure 9(a). Before the HPAB test, the pore size distribution of the specimen is more between 1000 and 20000 nm and 1~10 nm, and the pore size distribution in the range of 10~1000 nm is relatively less. Through multiple HPAB tests, the pore size distribution is an obvious "single peak" structure, and the number of pores in the range of 1000~20000 nm increases significantly Figure 9(b).

It can be seen from Figure 10 that the pore surface of the specimen is relatively flat, and the closed and semiclosed pores are well developed before the HPAB test Figure 10(a). The micropore cracks can be observed in the specimen after the one shock from HPAB test. The main reason is that the stress wave causes a dislocation pile-up in the internal medium of the specimen, which promotes the nucleation and development of closed pores and semiclosed pores to form microcracks Figure 10(b). Compared with after the one shock from HPAB test, more microcracks can be detected in the specimen after the 3rd HPAB test, and the distribution of microcracks is more random. The main reason is that with the increase of the number of HPAB tests, the dislocation pile-up effect is produced by stress wave, which causes irregular sliding of microcracks and further forms a large number of randomly distributed microcracks Figure 10(c). The

(a) After the one shock from HPAB

(b) After the three shock from HPAB

(c) After the five shock from HPAB

Figure 8: Surface rack evolution of specimen under multiple HPAB.

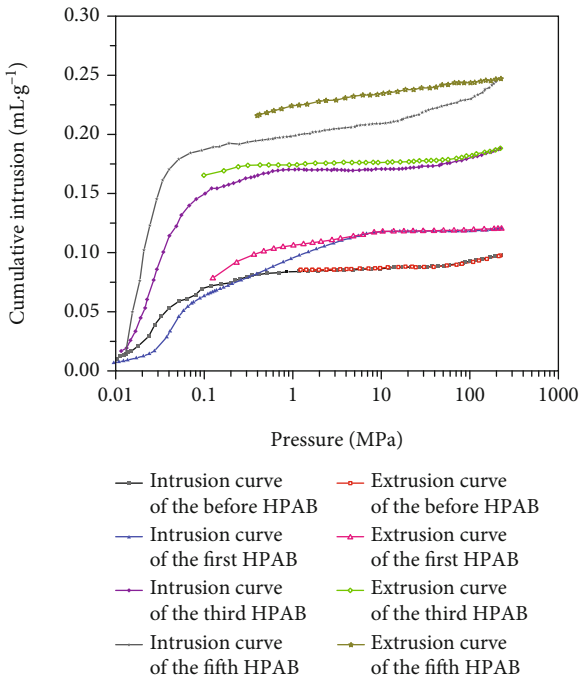

(a) Mercury intrusion and retraction curve

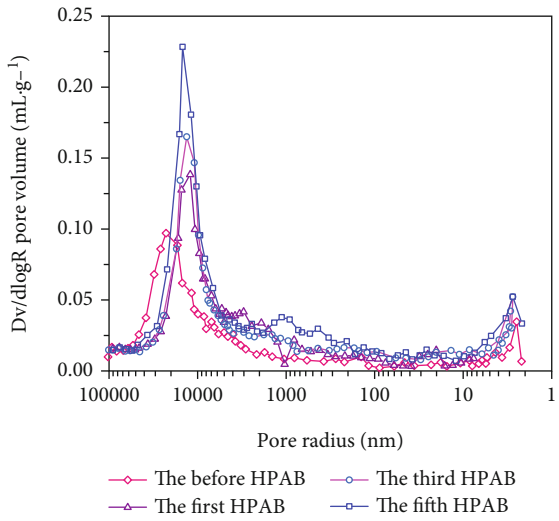

(b) Pore size distribution

Figure 9: Mercury intrusion and retraction curve and pore size distribution of the specimen under multiple HPAB tests.

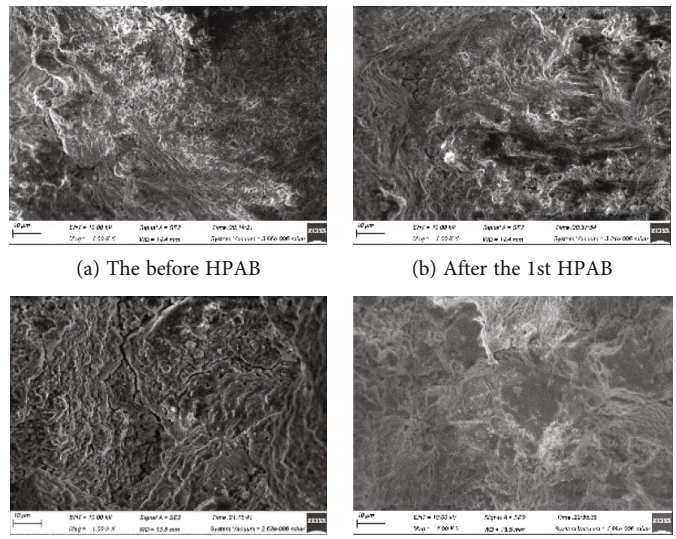

(a) The before HPAB (b) After the 1st HPAB

(c) After the 3rd HPAB (d) After the 5th HPAB

Figure 10: The comparison of SEM images under multiple HPAB tests.

connectivity of microcracks is enhanced in the specimen after the five shocks from HPAB test. The main reason is that the stress concentration of the microcrack tip factor is caused by multiple HPAB tests, which improves the development and penetration of randomly distributed microcracks and finally forms macrocracks Figure 10(d).

5. Conclusions

In this paper, the variation of stress field, cumulative damage evolution, and dynamic response of coal under multiple HPAB tests are studied by using the self-designed HPAB test system. The pore size distribution and pore structure evolution of specimens before and after the HPAB test are analyzed by MIP test and SEM technology, and the following conclusions are drawn:

(1) The stress wave generated by HPAB has a great impact on the near zone. After multiple HPAB, the damage value at the place 50 mm away from the blasthole increases by 3.91 times compared with the one shock from HPAB, and the strain peak and vibration velocity are reduced by 17.86% and 63.05%, respectively. With the increase of distance from the blasthole, the internal damages of the specimens in the middle and far zones are mainly driven by the stress wave and the high-pressure air, and the strain peak, vibration velocity, and damage degree gradually decrease

(2) With the increase of shock times in HPAB tests, the attenuation law of stress waves in coal is roughly similar. The attenuation indexes of strain under five shock from HPAB tests are 1.304, 1.161, 1.431, 1.511, and 1.728, respectively; the stress wave attenuation index decreases at first and then increases; the damages degree of the middle and far zones increase slowly in the first few shocks and then increase rapidly. The site coefficient (k) shows an overall decreasing trend, whereas the attenuation coefficient (α) tends to increasing

(3) With the increase of shock times in HPAB tests, the semi-closed pores and open pores in the coal are evolved from closed pores. Compared with unshocked specimen, the cumulative mercury injection and pore volume increased by 152.04% and 135.05%, respectively. The pore size distribution is an obvious "single peak" structure, and the number of pores in the range of 1000~20000 nm increases significantly. The stress concentration of the microcrack tip factor is caused by multiple HPAB tests, which improves the development and penetration of randomly distributed microcracks

Data Availability

The data used to support the findings of this study are available from the corresponding author upon request.

Conflicts of Interest

The authors declare that there are no conflicts of interest regarding the publication of this paper.

Acknowledgments

This study was supported by the National Natural Science Foundation of China (No. 51874123 and No. 52130403) and the Henan Research Program of Foundation and Advanced Technology (No. 162300410032).

References

[1] X. L. Yang, G. C. Wen, H. T. Sun et al., "Environmentally friendly techniques for high gas content thick coal seam stimulation—multi-discharge CO_2 fracturing system," *Journal of Natural Gas Science and Engineering*, vol. 61, pp. 71–82, 2019.

[2] S. L. Kong, Y. P. Cheng, T. Ren, and H. Liu, "A sequential approach to control gas for the extraction of multi-gassy coal seams from traditional gas well drainage to mining-induced stress relief," *Applied Energy*, vol. 131, pp. 67–78, 2014.

[3] Y. Xue, J. Liu, X. Liang, S. Wang, and Z. Ma, "Ecological risk assessment of soil and water loss by thermal enhanced methane recovery: numerical study using two-phase flow simulation," *Journal of Cleaner Production*, vol. 334, article 130183, 2022.

[4] B. Q. Lin, F. Z. Yan, C. J. Zhu et al., "Cross-borehole hydraulic slotting technique for preventing and controlling coal and gas outbursts during coal roadway excavation," *Journal of Natural Gas Science and Engineering*, vol. 26, pp. 518–525, 2015.

[5] C. Zhang, E. Wang, J. Xu, and S. Peng, "A new method for coal and gas outburst prediction and prevention based on the fragmentation of ejected coal," *Fuel*, vol. 287, article 119493, 2021.

[6] Y. Xue, J. Liu, P. G. Ranjith, Z. Zhang, F. Gao, and S. Wang, "Experimental investigation on the nonlinear characteristics of energy evolution and failure characteristics of coal under different gas pressures," *Bulletin of Engineering and the Environment*, vol. 81, no. 1, p. 38, 2022.

[7] Y. Li, Y. B. Wang, S. Z. Meng, X. Wu, C. Q. Tao, and W. K. Xu, "Theoretical basis and prospect of coal measure unconventional natural gas co-production," *Journal of China Coal Society*, vol. 45, no. 4, pp. 1406–1418, 2020.

[8] S. K. Sinha and S. D. Gupta, "A geological model for enhanced coal bed methane (ECBM) recovery process: a case study from the Jharia coalfield region, India," *Journal of Petroleum Science and Engineering*, vol. 201, article 108498, 2021.

[9] B. Huang and P. Li, "Experimental investigation on the basic law of the fracture spatial morphology for water pressure blasting in a drillhole under true triaxial stress," *Rock Mechanics and Rock Engineering*, vol. 48, no. 4, pp. 1699–1709, 2015.

[10] A. Vengosh, R. B. Jackson, N. Warner, T. H. Darrah, and A. Kondash, "A critical review of the risks to water resources from unconventional shale gas development and hydraulic fracturing in the United States," *Environmental Science and Technology*, vol. 48, no. 15, pp. 8334–8348, 2014.

[11] S. L. Brantley, D. Yoxtheimer, S. Arjmand et al., "Water resource impacts during unconventional shale gas development: the Pennsylvania experience," *International Journal of Coal Geology*, vol. 126, no. 1, pp. 140–156, 2014.

[12] J. Liu, Y. Xue, Q. Zhang, H. Wang, and S. Wang, "Coupled thermo-hydro-mechanical modelling for geothermal doublet system with 3D fractal fracture," *Applied Thermal Engineering*, vol. 200, article 117716, 2022.

[13] Y. X. Cao, J. S. Zhang, H. Zhai, G. Fu, L. Tian, and S. Liu, "CO_2 gas fracturing: a novel reservoir stimulation technology in low permeability gassy coal seams," *Fuel*, vol. 203, pp. 197–207, 2017.

[14] S. B. Hu, S. G. Pang, and Z. Y. Yan, "A new dynamic fracturing method: deflagration fracturing technology with carbon dioxide," *International Journal of Fracture*, vol. 220, no. 1, pp. 99–111, 2019.

[15] P. Hou, F. Gao, Y. Ju et al., "Experimental investigation on the failure and acoustic emission characteristics of shale, sandstone and coal under gas fracturing," *Journal of Natural Gas Science and Engineering*, vol. 35, pp. 211–223, 2016.

[16] S. T. Zhou, X. D. Luo, N. Jiang, Z. Zhang, and Y. K Yao, "A review on fracturing technique with carbon dioxide phase transition," *Chinese Journal of Engineering*, vol. 43, no. 7, pp. 883–893, 2021.

[17] J. H. Yang, W. B. Lu, Q. H. Jiang, C. Yao, and C. B. Zhou, "Frequency comparison of blast-induced vibration per delay for the full-face millisecond delay blasting in underground opening excavation," *Tunnelling and Underground Space Technology*, vol. 51, pp. 189–201, 2016.

[18] P. Huai-de, L. Dun-wen, C. Fu-jiao, and J. Ying-hua, "Test on high pressure gas expansion rock fragmentation in hard rock tunnel," *Rack and Soil Mechanics*, vol. 39, no. 1, pp. 242–248, 2018.

[19] S. P. Singh, "Non-explosive applications of the PCF concept for underground excavation," *Tunnelling and Underground Space Technology*, vol. 13, no. 3, pp. 305–311, 1998.

[20] Q. Li, X. Liu, Z. Wu, and X. Xie, "Application of liquid CO2 phase change rock breaking technology in metro foundation pit excavation," *Journal of Railway Science and Engineering*, vol. 15, no. 1, pp. 163–169, 2018.

[21] A. Parsakhoo, M. Lotfalian, and S. A. Hosseini, "Forest roads planning and construction in Iranian forestry," *Journal of Civil Engineering and Construction Technology*, vol. 1, no. 16, pp. 14–18, 2010.

[22] A. Parsakhoo and M. Lotfalian, "Demolition agent selection for rock breaking in mountain region of Hyrcanian forests," *Research Journal of Environmental Sciences*, vol. 3, no. 3, pp. 384–391, 2009.

[23] L. Y. Chi, Z. X. Zhang, A. Aalberg, J. Yang, and C. C. Li, "Measurement of shock pressure and shock-wave attenuation near a blast hole in rock," *International Journal of Impact Engineering*, vol. 125, pp. 27–38, 2019.

[24] W. Yuan, W. Wang, X. Su et al., "Numerical study of the impact mechanism of decoupling charge on blasting-enhanced permeability in low-permeability sandstones," *International Journal of Rock Mechanics and Mining Sciences*, vol. 106, pp. 300–310, 2018.

[25] L. Wang, B. Yao, H. Xie et al., "CO_2 injection-induced fracturing in naturally fractured shale rocks," *Energy*, vol. 139, pp. 1094–1110, 2017.

[26] L. J. Chen, J. M. Feng, and X. C. Wu, "Experimental research on transient rock breaking characteristics of high-energy gas," *Chinese Journal of Rock Mechanics and Engineering*, vol. 39, no. S2, pp. 3271–3277, 2020.

[27] J. Gao, H. Wang, W. Qin, Q. Ma, and G. Yang, "Experimental study on high-pressure air blasting fracture for coal and rock mass," *Advances in Civil Engineering*, vol. 2019, no. 12, Article ID 9613563, pp. 1–10, 2019.

[28] S. T. Zhou, N. Jiang, X. He, and X. Luo, "Rock breaking and dynamic response characteristics of carbon dioxide phase transition fracturing considering the gathering energy effect," *Energies*, vol. 13, no. 6, p. 1336, 2020.

[29] F. Wu, X. Wei, Z. Chen et al., "Numerical simulation and parametric analysis for designing high energy gas fracturing," *Journal of Natural Gas Science and Engineering*, vol. 53, pp. 218–236, 2018.

[30] Y. Bai, L. Sun, and C. H. Wei, "A coupled gas flow-mechanical damage model and its numerical simulations on high energy gas fracturing," *Geofluids*, pp. 1–14, 2020.

[31] Y. Lei, J. J. Liu, and S. N. Zhang, "Permeability improvement technology by cracking coal seam with CO2 phase transition," *Journal of Engineering Geology*, vol. 25, no. 1, pp. 215–221, 2017.

[32] Y. Liu, T. Zhang, and X. T. Liu, "Analysis of the stress wave effect during coal breakage by a high-pressure abrasive air jet," *Advances in Mechanical Engineering*, vol. 10, no. 6, p. 2072047318, 2018.

[33] X. Huang, Q. Y. Li, X. A. Wei et al., "Indoor test system for liquid CO2 phase change shock wave pressure with PVDF sensors," *Sensors*, vol. 20, no. 8, p. 2395, 2020.

[34] G. D. Zhang, Y. Zhao, X. Wang et al., "A manganin thin film ultra-high pressure sensor for microscale detonation pressure measurement," *Sensors*, vol. 18, no. 3, p. 736, 2018.

[35] M. Goodarzi, S. Mohammadi, and A. Jafari, "Numerical analysis of rock fracturing by gas pressure using the extended finite element method," *Journal of Natural Gas Science and Engineering*, vol. 36, pp. 1253–1263, 2016.

[36] C. H. Wei, W. C. Zhu, Q. L. Yu, T. Xu, and S. Jeon, "Numerical simulation of excavation damaged zone under coupled thermal, mechanical conditions with varying mechanical parameters," *International Journal of Rock Mechanics and Mining Sciences*, vol. 75, pp. 169–181, 2019.

[37] W. C. Zhu, D. Gai, C. H. Wei, and S. G. Li, "High-pressure air blasting experiments on concrete and implications for enhanced coal gas drainage," *Journal of Natural Gas Science and Engineering*, vol. 36, pp. 1253–1263, 2016.

[38] P. Wei, C. W. Huang, X. L. Li, S. Peng, and Y. Lu, "Numerical simulation of boreholes for gas extraction and effective range of gas extraction in soft coal seams," *Energy Science and Engineering*, vol. 7, no. 5, pp. 1632–1648, 2019.

[39] Y. Liu, J. Zhang, J. P. Wei, and X. Liu, "Optimum structure of a laval nozzle for an abrasive air jet based on nozzle pressure ratio," *Power Technology*, vol. 364, no. 3, pp. 343–362, 2020.

[40] X. Song, G. D. Wang, and H. Ma, "Mechanism and mathematical model of the continuous process of gas jet breaking coal," *Journal of China Coal Society*, vol. 45, no. 9, pp. 3176–3185, 2020.

[41] X. F. Xie, X. B. Li, and Q. Y. Li, "Liquid CO2 phase-transforming rock fracturing technology in pile-well excavation," *Journal of Central South University (Science and Technology)*, vol. 49, no. 8, pp. 1350–1356, 2018.

[42] X. Xia, H. B. Li, and X. W Wang, "Comparison analysis of ground vibrations induced by CO2 gas fracturing and explosive blasting," *Chinese Journal of Rock Mechanics and Engineering*, vol. 40, no. 7, pp. 1350–1356, 2021.

[43] H. B. Chu, X. L. Yang, and W. M. Liang, "Study on the damage fracture process and mechanism of coal blasting," *Journal of Mining & Safety Engineering*, vol. 35, no. 2, pp. 410–414, 2018.